A simplified method for estimating the permanent accumulated rotation of an offshore wind turbine monopile throughout its design life

Hongwang Ma [a],[*], Xuening Chang [b], Yawen Deng [a], Jun Yang [c]

[a] Department of Civil Engineering, Shanghai Jiao Tong University, Shanghai, 200240, China
[b] Shanghai Qiyuan Green Power Technology Co., LTD, Shanghai, China
[c] Department of Civil Engineering, The University of Hong Kong, Hongkong, China

A B S T R A C T

The permanent accumulated rotation is of great importance to the design of monopile foundations for offshore wind turbines because it is critical to the final dimensions of the monopile as well as its cost. Although design specifications require that the permanent accumulated rotation meet tolerances, they do not provide engineers with an appropriate method to calculate this value. This paper proposes a simplified method for estimating the permanent accumulated rotation of a monopile throughout its design life. To establish this method, a series of 1-g model tests were conducted in medium-dense sand to investigate the accumulative tendency of monopile rotation under typhoon and non-typhoon conditions. The results showed that the total accumulated rotation was mainly caused by typhoon events, further indicating that the static rotation generated by the maximum load magnitude among typhoon load sequences may maintain a certain proportional relationship with it. Then, the procedure for determining the two parameters in the method was illustrated by an NREL 5 MW wind turbine mounted on a monopile at a water depth of 28 m in the northern South China Sea. This method can provide a convenient tool for calculating the permanent rotation of a monopile foundation throughout its design life.

1. Introduction

Monopile foundations are currently the most common form of foundation for offshore wind turbines in shallow to moderate water depths (Gupta and Basu, 2020). During the typical 20–25 years operational life of an offshore wind turbine, a monopile foundation would be subjected to about 10^7-10^9 load cycles with low and intermediate amplitudes due to a combination of wind, waves, and current, as well as a small number of load cycles with large amplitudes caused by strong storm events (Abadie et al., 2019; Ma et al., 2021). These cyclic loads acting on the pile may result in possible hardening or softening of the surrounding soil, ultimately leading to permanent accumulated rotation, changes in the stiffness and damping of the monopile foundation (LeBlanc et al., 2010a; Schafhirt et al., 2016; Abadie et al., 2019). Among these changes, permanent accumulated rotation is of particular concern as it is critical to the final monopile dimensions as well as cost, and is typically specified by turbine manufacturers to tight tolerances (Wang and Larsen, 2019; Rathod et al., 2021; Richards et al., 2021). DNVGL (2018) guideline recommends that the total rotation at the seabed should not exceed a tolerance of 0.5°, derived from an installation

tolerance of 0.25° and a permanent accumulated rotation at seabed of 0.25°, but does not provide an appropriate methodology for calculating this value.

In current design practice, the typical p-y methods presented in API (2014) and DNVGL (2018) are generally considered to be limited in predicting the accumulated rotation of monopile foundations under long-term cyclic loading (Arshad and O'Kelly, 2016; Frick and Achmus, 2020). Hence, in order to obtain better methods for predicting the accumulated cyclic rotation, extensive studies have been conducted on the behavior of monopile foundations under cyclic lateral loading using small-scale 1-g (LeBlanc et al., 2010a, 2010b; Cuéllar, 2011; Abadie, 2015; Frick and Achmus, 2020) or centrifuge model tests (Klinkvort and Hededal, 2013; Truong et al., 2019; Li et al., 2020) or large-scale field tests (Li et al., 2015; Byrne et al., 2019) and numerical simulations (Barari et al., 2017; Ma et al., 2017; Le et al., 2021). Although the results of large-scale field tests are considered more reliable, they are difficult to implement due to their extremely high cost. Numerical studies are still in a state of development or need further validation (Frick and Achmus, 2020). Therefore, most approaches for estimating the accumulated rotation (displacement) are based on small-scale model tests. LeBlanc

et al. (2010a) studied the long-term cyclic response of rigid piles in dry sand by means of 1-g model tests involving cyclic loading numbers from 7000 to 65,000. The cyclic loading was characterized by two normalized parameters, namely the cyclic load magnitude ratio and the cyclic load ratio, respectively. A complete dimensionless framework was presented for the scaling of the laboratory tests and applied to interpret the test results, which was widely used by subsequent researchers (Abadie, 2015; Nanda et al., 2017; Ma et al., 2021). Based on the tests performed, a power law function to predict the permanent accumulated rotation of the pile head with increasing number of cycles was proposed. Cuéllar (2011) carried out a series of 1-g physical model tests on a reduced scale (1:100) of a stiff pile under cyclic lateral loads of up to 5 million loading cycles. The number of load cycles adopted in these tests most closely approximates the actual number of load cycles that the monopile foundation will withstand during its design life in the available published experimental studies. A generalized form of the log-linear accumulation law was found to provide a more accurate estimation of the permanent displacements in the very high cyclic range ($N > 10^6$). Abadie (2015) conducted a series of 1-g laboratory floor model tests on stiff piles under long-term continuous and multi-amplitude lateral cyclic loading in dry sand. The scaling law adopted in this study follows that proposed by LeBlanc et al. (2010a). Similar to previous findings (LeBlanc et al., 2010a, 2010b; Nicolai and Ibsen, 2014), under long-term amplitude cyclic loading, the accumulated rotation increases with the number of cycles and can be well fitted using the proposed empirical power law of LeBlanc et al. (2010a) within the first 10,000 cycles. Under multi-amplitude cyclic loading conditions, the total accumulated rotation is mainly due to the maximum magnitude load series caused by extreme storm-type events (e.g. typhoon or hurricane). This phenomenon has been identified in other studies in recent years (Barari et al., 2017; Wang and Larsen, 2019; Ma et al., 2021). To extensively investigate the effects of cyclic load ratio, load eccentricity and pile embedment length on pile displacement accumulation, Frick and Achmus (2020) conducted a series of small-scale 1-g model tests on laterally loaded monopiles in medium-dense sand. Their test results confirmed the suitability of the power function for approximating and extrapolating the cyclic pile displacement accumulation for load cycle number of a number of load cycles $N > 100$. In the 1-g experiments described above, it is difficult to simulate the stress level that is completely consistent with the full-scale conditions. Therefore, several centrifuge experiments at N-g have been carried out to investigate the accumulated deformation of monopiles under long-term cyclic loading. The results of these centrifuge tests show that the evolution of accumulated deformation is similar to that under 1-g conditions, and the ratcheting index may be smaller than the value obtained from the 1-g model test (Nicolai and Ibsen, 2014; Richards et al., 2021). However, the number of cycles of previous centrifuge model tests is limited and difficult to extend to a large cyclic number, mainly constrained by the control system of the test apparatus and the experimental cost (Abadie, 2015).

Although many methods have been proposed to predict the accumulated rotation of monopiles due to long-term cyclic loading, most of them are independent of the metocean conditions and are complicated for engineers to use. According to the statistics from 1977 to 2018, China may encounter 7 to 8 typhoon passes each year, and the typhoon resistant design is critical for the offshore wind turbines in China (Wang et al., 2022), especially for offshore wind farms located in the South China Sea. In this study, empirical formulas for estimating the accumulated rotation of monopiles subjected to typhoon loads and long-term small-amplitude loads are obtained from a series of 1-g model tests. Based on these empirical formulas, a simplified method for predicting the total accumulated rotation during the service life of a monopile is then established. The main idea of this method is to estimate the permanent accumulated rotation of monopiles caused by long-term cyclic loading based on the monotonic rotation under storm loads and the site correlation coefficient. Lastly, taking the offshore area in the northern part of the South China Sea as a case study, the process of calculating the

site correlation coefficient in this area is described in detail, and the calculation formula for estimating the accumulated rotation of a monopile during its design life that is applicable to this area is obtained.

2. Experimental test setup and procedures

2.1. Scaling considerations

In the reference prototype, a monopile foundation with a diameter of 6 m was used for the NREL 5-MW offshore wind turbine. The monopile foundation was embedded with a length of 36 m and a water depth of 30 m. 1-g small-scale model tests were conducted in the laboratory. Considering the similarity between the model test results and the prototype, this paper adopts the dimensionless framework proposed by LeBlanc et al. (2010a) to analyze the model test results. The dimensionless form of each parameter is summarized in Table 1.

2.2. Test equipment

The geometric similarity ratio between the model pile and the prototype pile was 1:100. The model pile was made of an open-ended aluminum tube with a length of 0.8 m, an outer diameter of 60 mm and a wall thickness of 2 mm. The elastic modulus of this aluminum pile was 70 GPa, which was tested by the simply supported method (Long and Bao, 1988). The model pile had an embedded length of 360 mm and a loading point height of 280 mm above the mudline. The saturated sand was prepared in a cylindrical stainless steel tank with an inner diameter of 600 mm, a height of 800 mm and a wall thickness of 3 mm. The inner diameter of the tank was 10 times of the outer diameter of the model pile. According to Richards et al. (2020), the lateral boundary effects are expected to be negligible. A 150 mm thick layer of highly permeable gravel was placed at the bottom of the tank, and a 600 mm thick layer of sand was placed at the top, separated by a geotextile. To ensure a homogenous relative density within the tank, the sand was packed layer by layer, compressed by weight every 100 mm. The distance from the pile tip to the bottom of the sand is 4 times the pile diameter, which can be considered as unaffected by the bottom boundary (Abdel-Rahman and Achmus, 2005). A small hole equipped with a valve near the bottom of the steel tank was used to connect the inlet and outlet water pipes. A cross-sectional view of the saturated sand setup is shown in Fig. 1.

The experiments were carried out under fully saturated conditions using graded quartz sand (Fujian sand) (Wang et al., 2015) with a grain size distribution similar to that of the Berliner sand used in the study by Cuéllar (2011). In the tests, the sand density was set at 1.60 g/cm³ in each case, with a relative density of about 67%. The main properties of the sand were tested according to GB/T50123-1999 (2015) and are shown in Table 2. The dry sand was layered into the sand tank, and each layer was compacted to the marked position before the next layer was filled. After filling all layers of dry sand, water was slowly injected through a hose connecting the sand tank and the water tank, as shown in Fig. 1. The waterline was placed at a level of +20 mm above the mudline. To ensure complete saturation, no tests were performed until after a period of 24 h. In all tests, the sand was replaced from time to time.

Table 1
Non-dimensional parameters proposed by LeBlanc et al. (2010a).

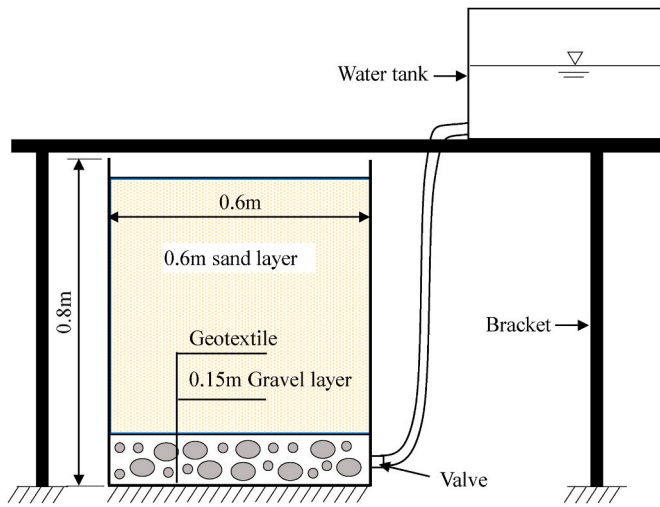| Parameter	Normalized form
Moment loading	$\widetilde{M} = \dfrac{M}{L^3 D \gamma'}$
Horizontal force	$\widetilde{F} = \dfrac{F}{L^2 D \gamma'}$
Rotation (degrees)	$\widetilde{\theta} = \theta \sqrt{\dfrac{p_a}{L \gamma'}}$
Displacement	$\widetilde{u} = \dfrac{u}{D} \sqrt{\dfrac{p_a}{L \gamma'}}$

Fig. 1. Schematic diagram of the saturated sand setup.

Table 2

Properties of model sand.

Property	Values
Maximum dry density, ρ_{max}: g/cm^3	1.73
Minimum dry density, ρ_{min}: g/cm^3	1.39
Specific gravity, G_s	2.65
Relative density, D_r: %	67
Mean particle size, D_{50}: mm	0.61
Coefficient of uniformity, C_u	2.41
Coefficient of curvature, C_c	0.82

As shown in Fig. 2, the loads were applied to the model pile using an electric servo actuator with a maximum stroke range of 200 mm, a maximum load capacity of 1000 N and a frequency range of 1 Hz. The actuator was placed on a steel frame and attached to the concrete floor. The electric servo actuator applied a horizontally monotonic and cyclic load at 280 mm above the mudline, and it was connected to the model pile by a rigid rod with hinged connections on both sides. The force exerted on the pile head was measured by an embedded tension/compression load cell. Two linear variable differential transformer (LVDT) displacement transducers were used to continuously measure pile displacements with an accuracy of ±0.03 mm, a range of 0–30 mm, and non-linearity within ±0.1%. These two LVDT measurements were used to calculate the lateral displacement of the pile at the mudline or the rotation of the pile. The displacement transducers and servo actuators were connected to synchronous data acquisition devices.
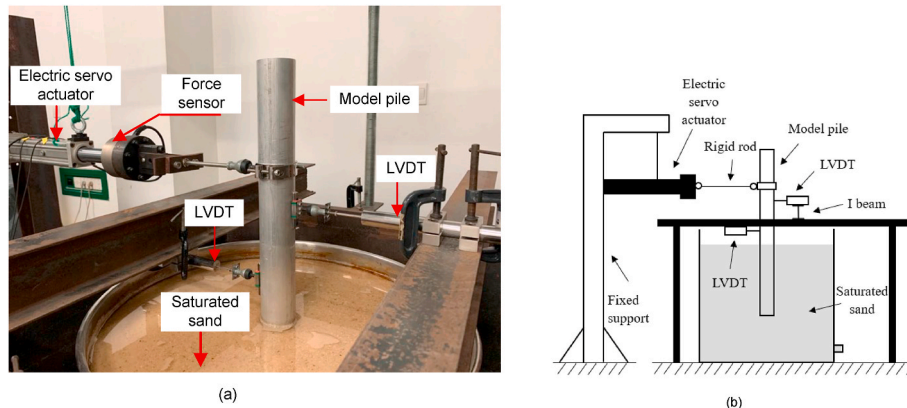
2.3. Test program

The testing involved monotonic and cyclic loading tests for determining the ultimate load capacity from static load-displacement response curves and providing insight into the evolution of the accumulated displacement of the monopile, respectively. In general, the load-displacement curve of rigid piles has no definite critical point of failure. In the model tests of Abadie et al. (2019) and Cuéllar (2011), the load corresponding to the pile displacement at the mudline reaching 0.1 times the pile diameter (0.1D) was used as the monotonic ultimate bearing capacity of the pile for the purpose of defining the ultimate bearing capacity of this test. The continuous loading rate was 5 N/min. According to the findings of Richards et al. (2020) regarding the loading rate, the effect of the loading rate was very limited in these tests with negligible effect. The sinusoidal cyclic loading frequency was 0.15 Hz. The two parameters proposed by LeBlanc et al. (2010a) were adopted to characterize cyclic loads:

$$\xi_b = \frac{M_{max}}{M_R} \quad (1)$$

$$\xi_c = \frac{M_{min}}{M_{max}} \quad (2)$$

where M_{max} and M_{min} are the maximum and minimum bending moments at the mudline. M_R is the ultimate moment capacity of the monopile.

According to the study by LeBlanc et al. (2010a), the fatigue design load was about 30% of the ultimate bearing capacity of the monopile. As a result, the value of ξ_b for the small-amplitude cyclic load in the tests was set to about 0.3, and for comparison, the two values of 0.2 and 0.4 were also used in the tests, and these ξ_b values are often used in model tests (LeBlanc et al., 2010a; Abadie et al., 2019; Frick and Achmus, 2020; Rathod et al., 2021). According to the study of M_{min}/M_{max} wind turbines under normal operational conditions by Jalbi et al. (2019), the value of ξ_c was uniformly set to 0.2 for long-term cyclic loads, which has also been adopted in this paper.

A typical typhoon structure consists of a typhoon periphery, a typhoon wall and a typhoon eye (Xiang et al., 2016). Since the actual wind and wave loads caused by typhoon have high irregularity, it is difficult to directly use these loads as design loads in the model tests, so the method level of transforming the time series of irregular cyclic loads into a series of regular loads (Wang and Larsen, 2019), where each section is a regular cyclic load of N cycles, was used to simplify the actual wind and wave loads. The procedure is shown in Fig. 3. The typhoon was divided into three sections in the test. The middle section represents the strongest area of the typhoon, and the two ends represent the periphery of the typhoon. Three typhoon classes were considered in the test. The value of ξ_b^{TY} in the middle section of each typhoon load was

Fig. 2. Experimental setup: (a) Picture of test setup with installed devices; (b) Sketch of testing rig and the loading actuator.
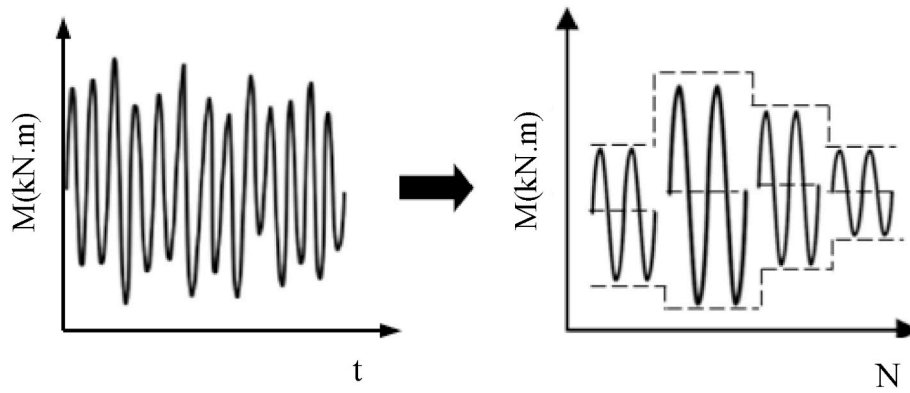
Fig. 3. Simplifying an irregular load series into load parcels of constant-amplitude cyclic loading.

set to 0.5, 0.6 and 0.7, respectively, considering that the worst expected transient loads are about 70% of the ultimate bearing capacity of the pile with a possibility of extreme events during the typhoon (LeBlanc et al., 2010a). The values of ξ_b for the two end sections under each typhoon load were taken as 0.4. Upon the passage of the typhoon, the wind speed exceeded the cut-out speed value and the wind turbine would be shut down to ensure safety. At this time, the wave loads become the dominant loads, so the value of ξ_c moves down and $\xi_c = 0$ is taken in the test. The number of load cycles for each typhoon is N = 12 for the middle section (Ma et al., 2021) and N = 300 for the two end sections. The loading parameters of the typhoons in the test are shown in Table 3. For simplicity of expression, the three typhoon conditions are numbered as A, B and C, respectively. All test programs are summarized in Table 4.

3. Test results and establishment of empirical functions

3.1. Monotonic test results

The results of the static normalized displacement at the mudline of the pile against relative to the applied normalized bending moment are plotted in Fig. 4. The pile displacement at the mudline was calculated from two LVDT measurements, and the bending moment was calculated by multiplying the applied lateral load by the load eccentricity (280 mm). As shown in Fig. 4, the results for ST1 and ST2 give $\widetilde{M}_R = 1.91$ ($M_R \approx 53.90$ N·m) and $\widetilde{M}_R = 1.85$ ($M_R \approx 52.20$ N·m, respectively, and the slight difference between the two values may be caused by a small density inconsistency. The average of the two values was taken as the normalized ultimate bending moment $\widetilde{M}_R = 1.88$ for the pile in all tests.

3.2. The effect of typhoon loading sequence on accumulated rotation

First, the effect of typhoon loading sequence on the accumulated rotation of monopiles was investigated. The relationship between the normalized accumulated rotation $\widetilde{\theta}$ and the number of cycles N in CT1-CT4 is depicted in Fig. 5, where the accumulated rotation is normalized according to dimensionless framework presented in Table 1. The values of $\widetilde{\theta}$ for CT1 and CT3 were 0.130 and 0.135, respectively, while those for CT2 and CT4 were 0.147 and 0.145, respectively. The final accumulated rotation was found to differ by only 3.8% (CT1, CT3) and 1.4% (CT2, CT4), indicating that the accumulated rotation is independent of the

Table 3
Characteristics of typhoon load sequences.

No.	Loading description (ξ_c =0)
A	$300 \times (\xi_b =0.4)$ - $12 \times (\xi_b^{ty} =0.7)$ - $300 \times (\xi_b =0.4)$
B	$300 \times (\xi_b =0.4)$ - $12 \times (\xi_b^{ty} =0.6)$ - $300 \times (\xi_b =0.4)$
C	$300 \times (\xi_b =0.4)$ - $12 \times (\xi_b^{ty} =0.5)$ - $300 \times (\xi_b =0.4)$

Table 4
Test program.

Test type	No.	Loading description	Number of cycles
Monotonic tests	ST1	Continuous (5N/min)	/
	ST2	Continuous (5N/min)	/
Cyclic loading that includes typhoons	CT1	$3000 \times [\xi_b = 0.2 , \xi_c = 0.2]$ - A - $3000 \times [\xi_b = 0.2 , \xi_c = 0.2]$	6612
	CT2	$3000 \times [\xi_b = 0.3 , \xi_c = 0.2]$ - A - $3000 \times [\xi_b = 0.3 , \xi_c = 0.2]$	6612
	CT3	A - $6000 \times [\xi_b = 0.2 , \xi_c = 0.2]$	6612
	CT4	A - $6000 \times [\xi_b = 0.3 , \xi_c = 0.2]$	6612
	CT5	A - $6000 \times [\xi_b = 0.4 , \xi_c = 0.2]$	6612
	CT6	B - $6000 \times [\xi_b = 0.2 , \xi_c = 0.2]$	6612
	CT7	B - $6000 \times [\xi_b = 0.3 , \xi_c = 0.2]$	6612
	CT8	B - $6000 \times [\xi_b = 0.4 , \xi_c = 0.2]$	6612
	CT9	C - $6000 \times [\xi_b = 0.2 , \xi_c = 0.2]$	6612
	CT10	C - $6000 \times [\xi_b = 0.3 , \xi_c = 0.2]$	6612
	CT11	C - $6000 \times [\xi_b = 0.4 , \xi_c = 0.2]$	6612
Long term cyclic loading	CT12	$11000 \times [\xi_b = 0.2 , \xi_c = 0.2]$	11000
	CT13	$11000 \times [\xi_b = 0.3 , \xi_c = 0.2]$	11000
	CT14	$11000 \times [\xi_b = 0.4 , \xi_c = 0.2]$	11000

typhoon loading sequence. A similar situation was also found in previous tests (LeBlanc et al., 2010b; Abadie et al., 2019), demonstrating the validity of Miner's rule and strain superposition theory in predicting the accumulated rotation under multi-amplitude load series. The accumulated rotation increment $\Delta \widetilde{\theta}$ caused only by typhoon was 0.105 and 0.111 for CT1 and CT3, respectively, compared with 0.102 and 0.106 for CT2 and CT4, respectively. It can be seen that the accumulated rotation increment caused only by typhoon at the beginning of the experiment is similar to the middle moment. Due to the random nature of the time period when the wind turbine is hit by typhoons during the service period, the typhoon loads are uniformly placed at the beginning of the test in this study for conservative considerations and convenience.
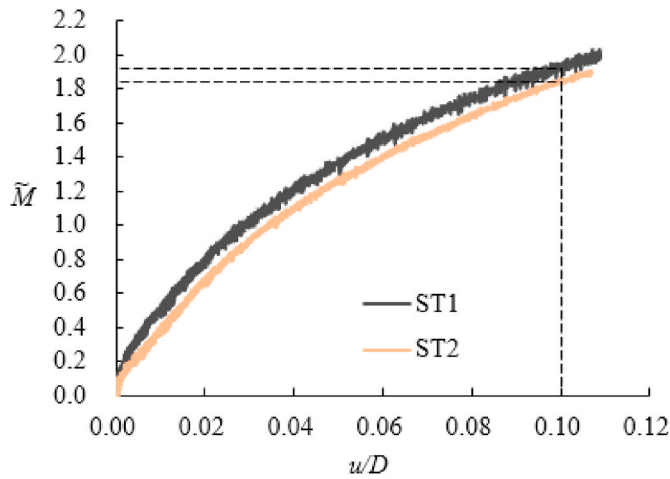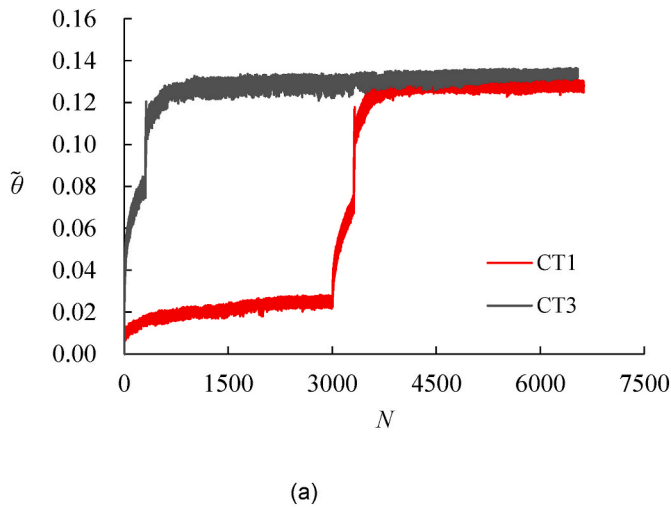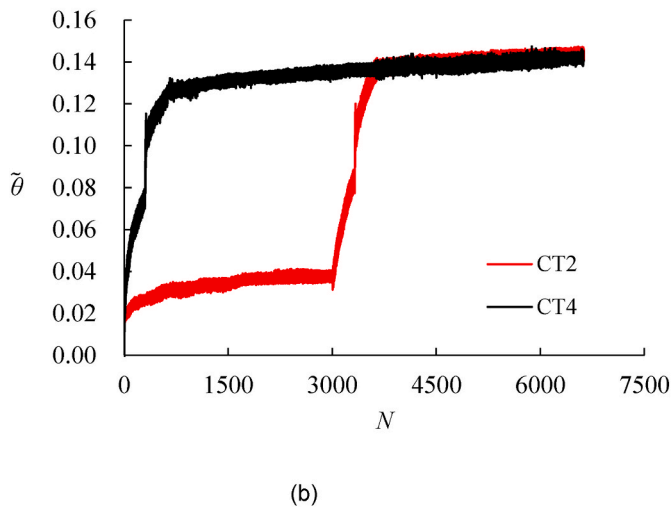
Fig. 4. Moment-displacement curve due to monotonic loading.

(a)

(b)

Fig. 5. Comparison of loading sequence test results of typhoon loads: (a) CT1 and CT3; (b) CT2 and CT4.

3.3. Accumulated rotation under cyclic tests with typhoon loading sequences

Nine cyclic tests (CT3-CT11) with typhoon loading sequences have been carried out. As shown in Table 3, CT3, CT4, and CT5 each consist of

typhoon A series, CT6, CT7, and CT8 each consist of typhoon B series, and CT9, CT10, and CT11 each consist of typhoon C series, at the initial stage of the loading process followed by constant cyclic loading with different small magnitudes. These tests were designed to study the accumulated rotational characteristics under typhoon events combined with small constant magnitude cyclic loads. Fig. 6(a) shows the evolution of pile accumulated rotation for CT3, CT4 and CT5, which can be roughly divided into two phases: the accumulated rotation increases rapidly to a high level after a typhoon loading sequence, and then slowly increases under small-amplitude cyclic loading. The rate of increase of the accumulated rotation under small-amplitude cyclic loads is positively correlated with the amplitude of cyclic loads (ξ_b). The accumulated rotation of CT6, CT7 and CT8 with typhoon B (Fig. 6(b)) and CT9,
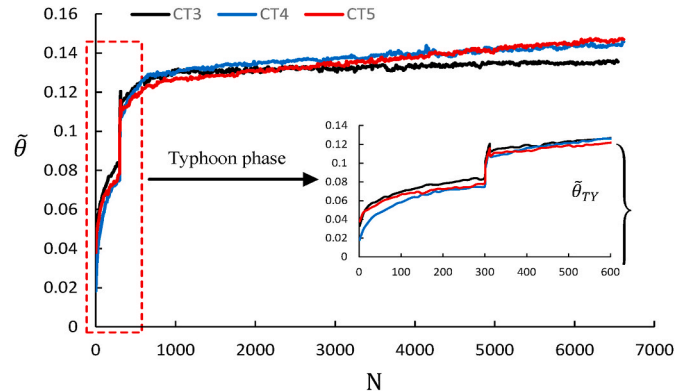
(a)
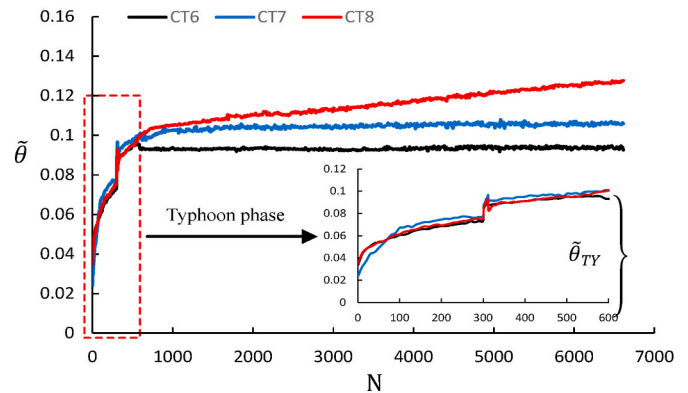
(b)
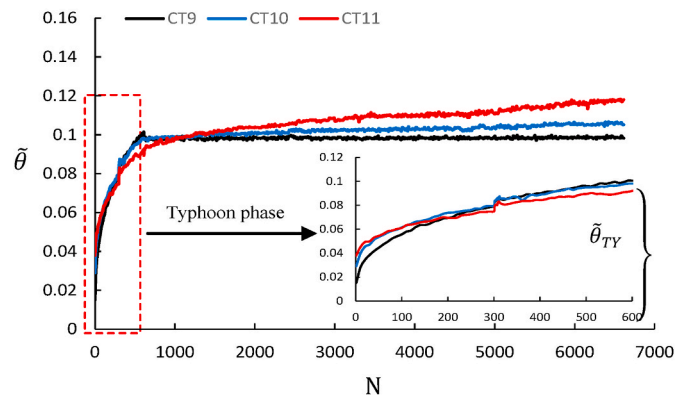
(c)

Fig. 6. Accumulated rotation due to typhoon loads: (a) Typhoon A; (b) Typhoon B; (c) Typhoon C.

CT10 and CT11with typhoon C (Fig. 6(c)) loading sequences have similar evolutionary trends to that of typhoon A (CT3, CT4 and CT5). Among them, an obvious difference is that the accumulated rotation generated by typhoon A is significantly larger than that generated by typhoon B and C. The ratio of the total accumulated rotation generated by each cyclic load test to the accumulated rotation generated by the corresponding typhoon loading sequence is shown in Table 5. It can be seen from Table 5 that the accumulated rotation is mainly caused by typhoon loads in all tests, especially when the load magnitude is small, such as cyclic loads like $\xi_b = 0.2$, and the accumulated rotation caused by typhoon loads accounts for more than 94.5%. This result is consistent with those published in the literature (LeBlanc et al., 2010b; Ma et al., 2021; Barari et al., 2017) that the total accumulated rotation is mainly caused by a few instances of extremely large load cycles.

3.4. Approximate methods for estimating the accumulated rotation caused by typhoon loads

As shown in Fig. 6, the evolution of accumulated rotation under typhoon loads is divided into three stages, often with a jump step in the middle part. The magnitude of the jump step increased with the maximum magnitude of the typhoon loads, resulting in a gradual increase in the accumulated rotation. In view of the small number of large-scale cyclic loads in the middle part of the typhoon, a larger accumulated rotation can be induced.

3.4.1. Method 1
To reflect the three-stage characteristics of the accumulated rotational evolution under typhoon loads, a piecewise function was fitted to each test and is shown as a dashed line (Fig. 7). The evolutionary trend before and after the transition was observed to be approximately coherent, so a function was fitted to the curve before the transition, and the cumulative rotation value after the transition was obtained by adding the incremental value of the transition to the function. Fitting the exponential trend line to the variation of $\frac{\widetilde{\theta}_{TY}}{\theta_{s,TY}}$ with the number of cycles (N) is in agreement with the method proposed by LeBlanc et al. (2010a).

$$\frac{\widetilde{\theta}_{TY}}{\widetilde{\theta}_{s,TY}} = \begin{cases} \eta_1 N^{\eta_2} & N \leq N_1 \\ \eta_1 N^{\eta_2} + \Delta\theta\left(\xi_b^{TY}, N_2\right) & N > N_1 \end{cases} \tag{3}$$

where $\widetilde{\theta}_{TY}$ is the normalized accumulated rotation of the typhoon load, $\widetilde{\theta}_{s,TY}$ is the normalized monotonic rotation corresponding to ξ_b^{TY}, the values of ξ_b^{TY} for Typhoon A, B, and C are 0.7, 0.6, and 0.5, respectively, and the rotations corresponding to $\widetilde{\theta}_{s,TY}$ are 0.065, 0.051, and 0.038, respectively (Fig. 8), η_1 and η_2 are the fitting coefficients, N_1 is the number of typhoon load cycles before the jump step, and $\Delta\theta(\xi_b^{TY}, N_2)$ is the value of the jump step, which is related to ξ_b^{TY} and N_2 of cyclic loads in the typhoon middle region. For Typhoon A, B and C, $\Delta\theta(\xi_b^{TY}, N_2)$ can be obtained from the test results. The fitting results are shown in Fig. 7, and the corresponding fitting functions are summarized in Table 6.

As shown in Fig. 7 and Table 6, this method is well fitted to the entire evolution of the accumulated rotation during the typhoon load series. However, engineers are more concerned with the total accumulated rotation rather than the specific cumulative process. Since this method requires the determination of multiple parameters in the calculation of the total accumulated rotation, it is more complicated for engineers. Therefore, a simpler method for calculating the total accumulated rotation under typhoon loads is proposed below.

3.4.2. Method 2
The test response during the typhoon series was fitted using an envelope exponential function instead of the piecewise function in Method 2. Based on observations of the accumulated rotational evolution in the tests (Fig. 6), the first 50 cycles before the jump step and the entire cycle after the jump step were selected from the $\widetilde{\theta}_{TY}/\widetilde{\theta}_{s,TY}$–N curve to establish the fitting function:

$$\widetilde{\theta}_{TY} = \beta_{TY}\left(\xi_b^{TY}\right) N^{\alpha_{TY}\left(\xi_b^{TY}\right)} \cdot \widetilde{\theta}_{s,TY} \tag{4}$$

where β_{TY} and α_{TY} are dimensionless coefficient functions related to ξ_b^{TY}, as shown in Table 7, and N is the total number of cycles for the typhoon series. As shown in Fig. 7, the fitting function differs significantly from the test response in the middle segment, especially for typhoon A and typhoon B, but provides a good fit for the total accumulated rotation of all typhoon series. The variation of β_{TY} and α_{TY} with the maximum magnitude of the typhoon series is plotted in Fig. 9, where β_{TY} and α_{TY} are obtained by fitting the relevant tests result, as shown in Table 7. The trend of β_{TY} and α_{TY} variation is clearly observed for the maximum magnitude of the typhoon load (ξ_b^{TY}): β_{TY} decreases with increasing ξ_b^{TY} and, on the contrary, α_{TY} increases with increasing ξ_b^{TY}. Two linear trend lines were fitted to the data in Fig. 9 to quantify the variation of β_{TY} and α_{TY} with ξ_b^{TY}, respectively, and are shown as a dashed line. The fitting lines are defined as:

$$\beta_{TY}\left(\xi_b^{TY}\right) = -1.2335\xi_b^{TY} + 1.2426 \tag{5}$$

$$\alpha_{TY}\left(\xi_b^{TY}\right) = 0.1925\xi_b^{TY} + 0.1128 \tag{6}$$

The accuracy of Eq. (4) has been verified by test data conducted by LeBlanc et al. (2010a). One of the test cases in LeBlanc's test program is $\xi_b^{TY} = 0.52$ and $\xi_c = 0$, which fall under the typhoon conditions defined in this paper. Based on the test results of LeBlanc et al. (2010a), $\widetilde{M}_R$ is 1.24 and $\widetilde{\theta}_{s,TY}$ is 0.012. According to Eqs. (5) and (6), $\beta_{TY}(0.52)$ and $\alpha_{TY}(0.52)$ are calculated as 0.6001 and 0.2129, respectively. Then, these two coefficients and $\widetilde{\theta}_{s,TY}$ are substituted into Eq. (4), and the normalized accumulated rotation of the monopile under typhoon loads is obtained, as shown in Table 8. This shows that the results calculated by Eq. (4) are in good agreement with the experimental results of LeBlanc et al. (2010a).

3.5. Accumulated rotation under long-term cyclic tests without typhoon load series

Three non-typhoon conditions, namely CT12, CT13 and CT14, were designed to study the evolutionary trend of accumulated rotation under long-term small constant magnitude cyclic loads. The cyclic magnitude ratios ξ_b were 0.2, 0.3 and 0.4 for CT12, CT13 and CT14, respectively. The relationship between the normalized accumulated rotation of the pile and the number of loading cycles for these three conditions are shown in Fig. 10. It can be seen that the evolutionary trend of the accumulated rotation is similar to that observed in previous studies (LeBlanc et al., 2010a; Achmus et al., 2019) and can be fitted using the exponential function proposed by LeBlanc et al. (2010a):

$$\widetilde{\theta}_{CYC} = \beta_{cyc}(\xi_b) N^{\alpha_{cyc}(\xi_b)} \cdot \widetilde{\theta}_{s,CYC} \tag{7}$$

where $\widetilde{\theta}_{CYC}$ is the normalized cumulative rotation caused by long-term

Table 5
Ratio of the accumulated rotation by typhoon to total accumulated rotation.

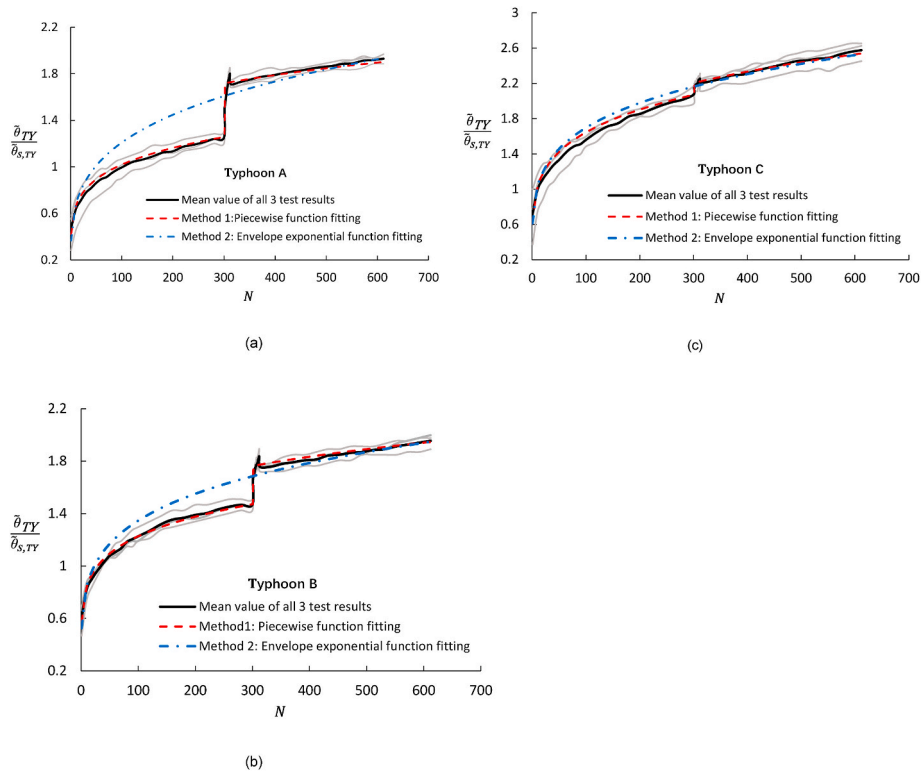| Test type	$\widetilde{\theta}$	$\widetilde{\theta}_{TY}$	$\widetilde{\theta}_{TY}/\widetilde{\theta}$
CT3	0.135	0.127	0.941
CT4	0.145	0.127	0.876
CT5	0.147	0.122	0.830
CT6	0.094	0.093	0.989
CT7	0.106	0.101	0.953
CT8	0.127	0.100	0.787
CT9	0.098	0.101	1.031
CT10	0.105	0.098	0.933
CT11	0.118	0.092	0.780

Fig. 7. Comparison of testing and fitting results: (a) Typhoon A; (b) Typhoon B; (c) Typhoon C.
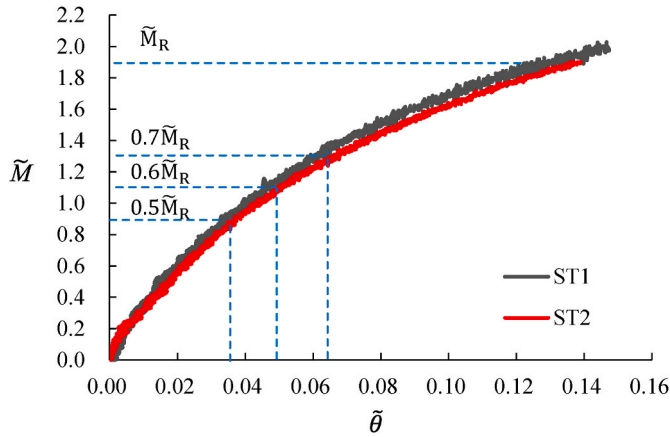

Fig. 8. The monopile monotonic $\widetilde{M} - \widetilde{\theta}$ curve.

Table 6
Empirical functions obtained by method 1.

Typhoon sequence	Fitting function
A	$\dfrac{\widetilde{\theta}_{TY}}{\widetilde{\theta}_{s,TY}} = \begin{cases} 0.423N^{0.191} & N \leq 300 \\ 0.423N^{0.191} + 0.461 & N > 300 \end{cases}$
B	$\dfrac{\widetilde{\theta}_{TY}}{\widetilde{\theta}_{s,TY}} = \begin{cases} 0.5716N^{0.1657} & N \leq 300 \\ 0.5716N^{0.1657} + 0.291 & N > 300 \end{cases}$
C	$\dfrac{\widetilde{\theta}_{TY}}{\widetilde{\theta}_{s,TY}} = \begin{cases} 0.625N^{0.21} & N \leq 300 \\ 0.6256N^{0.21} + 0.134 & N > 300 \end{cases}$

Table 7
Empirical formulas obtained by method 2.

Typhoon sequence	Fitting function	R^2
A	$\dfrac{\widetilde{\theta}_{TY}}{\widetilde{\theta}_{s,TY}} = 0.3659N^{0.2596}$	0.9632
B	$\dfrac{\widetilde{\theta}_{TY}}{\widetilde{\theta}_{s,TY}} = 0.525N^{0.2043}$	0.9822
C	$\dfrac{\widetilde{\theta}_{TY}}{\widetilde{\theta}_{s,TY}} = 0.613N^{0.2211}$	0.9830
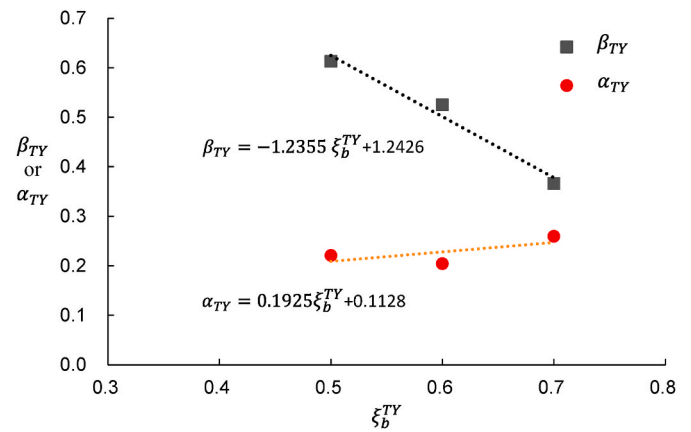
Fig. 9. Functions relating (a) β_{TY} and (b) α_{TY} to characteristics of cyclic load.ξ_b^{TY}

small cyclic loading, $\widetilde{\theta}_{s,CYC}$ is the normalized monotonic rotation corresponding to the maximum value of cyclic loads, which are 0.011, 0.019 and 0.027, respectively, and ξ_b is 0.2, 0.3 and 0.4, respectively. β_{cyc} and α_{cyc} are dimensionless functions, which depend on the cyclic load

magnitude ratio ξ_b, as follows:

$$\beta_{cyc}(\xi_b) = 1.7055\xi_b + 0.1555 \tag{8}$$

Table 8
Comparison between calculated and test results ($\Delta\theta_{0.52}/\theta_{s,0.52}$)

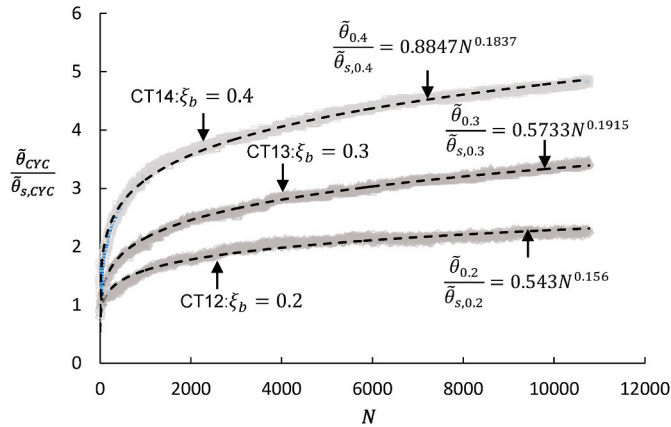| N	calculated value	test value (LeBlanc et al., 2010a)
1000	1.58	1.60
2000	2.00	2.00
4000	2.50	2.50
6000	2.83	2.80
8000	3.08	3.00
10,000	3.25	3.10

Fig. 10. Comparison between testing and fitting results for CT12, CT13 and CT14.

$$\alpha_{cyc}(\xi_b) = 0.1385\xi_b + 0.1355 \tag{9}$$

4. Simplified method for estimating the accumulated rotation of monopile foundations during their lifetime

By comparing the experimental results of typhoon loads and long-term small cyclic loads, it can be found that typhoon loads are the dominant factor causing monopile accumulation rotation compared to long-term small cyclic loads. This phenomenon is consistent with the findings of Abadie et al. (2019) and Barari et al. (2017). Since typhoon is the main factor causing accumulated rotation of the monopile foundation, the total accumulated rotation can be estimated by multiplying the accumulated rotation caused by typhoon by the correction factor. To further simplify the calculation, the accumulated rotation due to typhoon can be determined by multiplying the rotation obtained by monotonic loading of the maximum load corresponding to the typhoon sequence by the correction coefficient, as shown in Eq. (4). Based on above description, to simplify the estimation of the total accumulated rotation of the monopiles, the two normalized parameters K_{TYC} and K_{TYS} are defined by Eqs. (10) and (11), respectively.

$$K_{TYC} = \frac{\widetilde{\theta}_{total}}{\widetilde{\theta}_{TY}} \tag{10}$$

$$K_{TYS} = \frac{\widetilde{\theta}_{TY}}{\widetilde{\theta}_s^{\xi_b^{max}}} \tag{11}$$

where $\widetilde{\theta}_{total}$ is the normalized total accumulated rotation of the monopile during its service life, $\widetilde{\theta}_{TY}$ is the normalized accumulated rotation induced by the typhoon loading sequence, and $\widetilde{\theta}_s^{\xi_b^{max}}$ is the dimensionless monotonic rotation of the typhoon loading sequence corresponding to the maximum cyclic load amplitude (ξ_b^{max}).

The total normalized accumulated rotation is finally given as Eq. (12):

$$\widetilde{\theta}_{total} = K_{TYC} \cdot \widetilde{\theta}_{TY} = K_{TYC}K_{TYS}\widetilde{\theta}_s^{\xi_b^{max}} \tag{12}$$

where K_{TYC} and K_{TYS} are coefficients related to the site conditions and the wind turbine structure. The process of determining these two parameters is illustrated below with a case study.

5. Case study

This section illustrates how to obtain the specific values of K_{TYC} and K_{TYS} in Eq. (12) taking an offshore wind site in the northern part of the South China Sea as a case study. The NREL 5-MW wind turbine with a monopile foundation was chosen as the reference model (Jonkman et al., 2009). Its main characteristic properties are summarized in Table 9. The tower has a total length of 77.6 m, with an outer diameter of 3.87 m at the top and 6 m at the base, and is connected to the monopile via a transition piece. The monopile has a constant outer diameter and thickness of 6 m and 0.075 m, respectively. The tower base begins at an altitude of 10 m above mean sea level (MSL). The monopile extends to 36 m below the mudline. The material properties of the monopile and tower are based on S355 steel. For simplicity, the monopile is embedded in a medium dense homogeneous sandy soil with properties consistent with the sandy soil used in the model test in this paper (Table 2).

5.1. Horizontal ultimate capacity of the monopile

The horizontal ultimate capacity was determined by finite element static pushover analysis at a moment arm of 28 m. A numerical model of the prototype monopile was developed using the available FE software package ABAQUS 6.14. A circular soil domain with a diameter of 78 m (=12 D) and a depth of 60 m (=10 D) was modeled as shown in Fig. 11. The lower boundary was fixed against movements in all directions. It can be verified that these model dimensions are adequate to ensure that there are no artificial boundary effects on the behavior of soil-pile systems (Chang, 2021). The soil around the pile including the soil plug were constructed using the continuum element type (C3D8R). The steel pile was modeled using shell elements (S4R). The details of the FEM mesh are shown in Fig. 11. The material behavior of the monopile is assumed to be linearly elastic with Young's modulus $E_s = 210$ GPa and Poisson's ratio $\nu = 0.25$. Soil materials have been idealized using the Mohr-Coulomb model. The elasto-plastic behavior is characterized by Young's modulus, Poisson's ratio, cohesion c, internal friction angel φ' and dilation angle ψ, which are presented in Table 10. The soil was divided into 10 layers at a height of 6 m to vary the stiffness with depth, and Young's modulus of elasticity was estimated according to Eq. (13) (Achmus et al., 2009).

$$E_{soil} = k_s \sigma_{at} \left(\frac{\sigma}{\sigma_{at}}\right)^\lambda \tag{13}$$

where E_{soil} is the Young's modulus of the soil; $\sigma_{at} = 100$ kN/m^2 is the reference atmospheric stress, and σ is the current mean principal stress in the soil element under consideration. The parameters k_s and λ are 700

Table 9
Main parameters of the NREL 5 MW wind turbine (Jonkman et al., 2009).

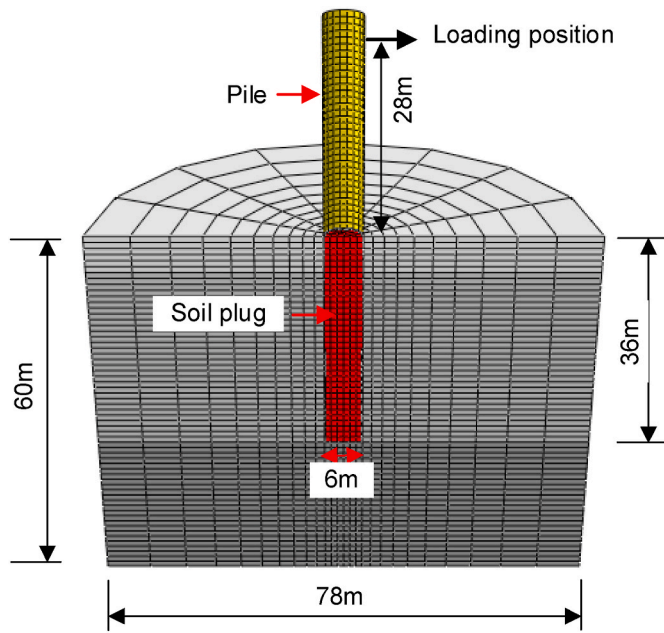| Item	Value
Rated Power (MW)	5
Number of blades	3
Rotor diameter (m)	126
Rated wind speed (m/s)	11.4
Cut-in, rated, cut-out wind speed (m/s)	3, 11.4, 25
Cut-in, Rated rotor speed (rpm)	6.9, 12.1
Rotor-nacelle assembly mass (kg)	350,000
Hub Height (m)	90

Fig. 11. 3D finite element model for prototype monopile.

and 0.55, respectively, for medium-dense sand (EAU, 2012).

The internal friction angle was chosen based on the relative density of the medium-dense sand used in the model test, which was approximately 38°, and the dilation angle was estimated to be $\psi = \varphi' - 30° = 8°$ (Achmus et al., 2019). To ensure computational convergence, a small value of c = 2 kPa was used.

In ABAQUS/Standard, the pile-soil interaction was modeled as a small sliding, surface-to-surface master/slave contact pair formulation. Hard contact and isotropic Coulomb friction models were available for the normal and tangential directions, respectively. Both normal and tangential contact constraints were enforced using the penalty method. The friction coefficient (μ) for the interface is taken as $\mu = \tan\left(\frac{2}{3}\varphi'\right)$.

The bending moment-displacement and rotation of the prototype monopile (Fig. 12) are used to determine the ultimate capacity and static monotonic rotation. As shown in Fig. 12, the horizontal ultimate capacity corresponding to 0.1D displacement of the mudline is 1200.08 MN m; when the static bending moment of each load case is determined, the corresponding static monotonic rotation of the monopile can be found from the bending moment-rotation curve.

5.2. Wind and waves characteristics

The probability distribution of wind speed in the northern South China Sea was referenced from Liao et al. (2018) and described by the 2-parameter Weibull distribution:

$$F(V_{W,10}) = 1 - \exp\left(-\left(\frac{V_{W,10}}{\beta_1}\right)^{\alpha_1}\right) \qquad (14)$$

where $V_{W,10}$ is the mean wind speed at a height of 10 m, and α_1 and β_1 are the shape and scale parameters, respectively. The values of $\alpha_1 = 1.94$ and $\beta_1 = 7.755$ are determined based on the measurements in the northern part of the South China Sea in the last decade (Liao et al., 2018). Corresponding to $V_{W,10}$, the effective wave height H_s and the

peak period T_P are estimated from Eqs. (15) and (16), as proposed by He and Zhang (2012) and Shu et al. (2012), respectively:

$$H_s = a + b\left(V_{W,10} - V_{W,x_i}\right) + \frac{c}{2}\left(V_{W,10} - V_{W,x_i}\right)^2 + \frac{d}{6}\left(V_{W,10} - V_{W,x_i}\right)^3 \qquad (15)$$

$$T_P = 5.497 \times H_S^{0.545} \qquad (16)$$

where a, b, c and d are fitting parameters, determined based on the measured values in the northern part of the South China Sea, which are 0, 0.4286, −0.0242 and 0.0015, respectively, and the reference wind speed $V_{W,x_i} = 15.55$ m/s (He and Zhang, 2012).

The reference height was set to 10 m above mean sea level, and the wind speed at the reference height was divided into wind speed intervals by 2 m/s from small to large, with the wind speed probability distribution having a total probability of 100% being established. There were 19 different load cases with different wind and wave combinations and occurrence probabilities, as shown in Table 11.

5.3. Wind load

In this paper, wind loads on the rotor and on the wind turbine tower are considered. The wind loads acting on the rotor are considered in two states, i.e., when the wind turbine is in a normal operating state and in a non-operating state. The wind load on the rotor in the operating mode can be estimated as (Arany et al., 2017):

$$F_{thrust} = \frac{1}{2}\rho_a A_R C_T V_{W,hub}^2 \qquad (17)$$

where F_{thrust} is the thrust force on the rotor, $\rho_a = 1.225$ kg/m³ is the air density, $A_R = 12445.3$ m² is the rotor area, $V_{W,hub}$ is the mean wind speed at the hub, and C_T is the thrust coefficient:

1) When the wind speed acting on the turbine rotor varies between the cut-in wind speed and the rated wind speed, C_T can be calculated as (Arany et al., 2017):

$$C_T = \frac{3.5\left(2V_{W,hub} - 3.5\right)}{V_{W,hub}^2} \approx \frac{7}{V_{W,hub}} \qquad (18)$$
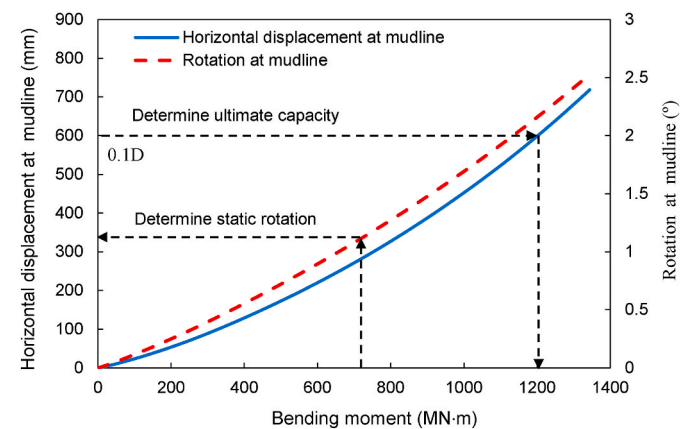

Fig. 12. Ultimate capacity and static rotation determined from monotonic static numerical analysis.

Table 10
Soil properties used in the model.

Type of sand	Unit weight (kN.m^{-3})	Poisson's ratio	Angle of friction (deg.)	Cohesion (kPa)	Friction coefficient	Angle of Dilatancy (deg.)
Medium dense	10.00	0.28	38	2	0.47	8

Table 11
Environmental states, based on data from Liao et al. (2018).

Load case	$V_{W,10}$ (m/s)	V_{hub} (m/s)	H_s (m)	T_P (s)	P_{state}
1	0–2	1.41	0.42	3.41	0.042522361
2	2–4	4.24	1.18	6.03	0.126373302
3	4–6	7.07	1.87	7.74	0.181713248
4	6–8	9.90	2.49	9.04	0.194471073
5	8–10	12.73	3.06	10.11	0.170027427
6	10–12	15.56	3.58	11.02	0.125763605
7	12–14	18.39	4.08	11.82	0.08000406
8	14–16	21.22	4.55	12.55	0.044157387
9	16–18	24.05	5.03	13.26	0.021252922
10	18–20	26.88	5.51	13.93	0.008946843
11	20–22	29.71	6.01	14.60	0.003300331
12	22–24	32.54	6.53	15.29	0.001067991
13	24–26	35.37	7.10	16.00	0.000303377
14	26–28	38.20	7.70	16.72	7.56751E-05
15	28–30	41.03	8.31	17.43	1.65781E-05
16	30–32	43.86	8.92	18.12	3.1895E-06
17	32–34	46.69	9.54	18.79	5.38847E-07
18	34–36	49.51	10.15	19.44	7.99243E-08
19	36–38	52.34	10.76	20.07	1.04054E-08

The thrust coefficient should not exceed 1.

2) When the wind speed acting on the turbine rotor varies between the rated wind speed V_R and the cut-out wind speed, assuming that the power remains stable, C_T is expressed as (Arany et al., 2017):

$$C_T = 3.5V_R(2V_R+3.5).\frac{1}{V_{W,hub}^3} \approx 7.\frac{V_R^2}{V_{W,hub}^3} \qquad (20)$$

3) When the wind speed is lower than the cut-in wind speed or higher than the cut-out wind speed, the blades will stop rotating, and the thrust force (Fan, 2016; Tang et al., 2018) on the blades is estimated as:

$$F_{thrust} = \frac{1}{2}\rho_a A_b C_T V_{W,hub}^2 \qquad (21)$$

where $A_b = 469.5 \ m^2$ is the projected area of the three blades. When the wind speed is higher than the cut-out wind speed, the thrust coefficient is 1.7 (Tang et al., 2018). In addition, when the wind speed is lower than the cut-in wind speed, the thrust coefficient is taken as 1.

The wind load on the tower depends on the variation of wind speed with height. The tower is equally divided into 10 segments and the wind load is treated as a concentrated load in the middle of the segment, and is estimated as follows:

$$F_{tower}^{H_i} = 0.5\rho_a C_s A_{tower}^{H_i} V_{wH_i}^2 \qquad (22)$$

where $F_{tower}^{H_i}$ is the wind load acting on the tower N at height H_i; $A_{tower}^{H_i}$ is the wind pressure area at height H_i in m^2; $C_s = 0.7$ is the shape coefficient of the tubular steel tower (Utsunomiya et al., 2014); H_i is the height above sea water level of segment i. A logarithmic profile is used to describe the wind shear phenomenon (van der Tempel, 2006):

$$V_{wi}(H_i) = V_{w,10}\frac{\ln\left(\frac{H_i}{H_0}\right)}{\ln\left(\frac{H_r}{H_0}\right)} \qquad (23)$$

where H_r is the reference height, $H_r = 10$ m, and H_0 is the surface roughness length (taken as 0.05 according to DNVGL (2016).

After determining the wind load on the rotor and tower, the total bending moment of the mudline caused by the wind is given by the following equation:

$$M_{wind} = M_{rotor} + M_{tower} = F_{thrust} \times (h_w + H_{hub}) + \sum_{i=1}^{10} F_{tower}^{Z_i} \times (H_i + h_w) \qquad (24)$$

where M_{wind} is the total bending moment of the mudline arising from the wind, M_{rotor} and M_{tower} are the bending moments of the mudline arising from the wind load of the rotor and tower, respectively, h_w is the water depth, and H_{hub} is the hub height.

5.4. Wave load

In order to accurately predict the wave loads on monopiles at all water levels, especially when considering extreme irregular sea conditions, the second-order Stokes wave theory combined with the Morison equation is used to calculate the wave loads on the structure (DNVGL, 2016). The horizontal force on a vertical element of the monopile at level z (Fig. 13) is expressed as:

$$dF = dF_D + dF_M = \frac{1}{2}C_D\rho_w Du_x|u_x|dz + C_M\rho_w\frac{\pi D^2}{4}\frac{\partial u_x}{\partial t}dz \qquad (25)$$

The total horizontal force F_{wave} (Bisoi and Haldar, 2014) and bending moment M_{wave} at the mudline are then given by integration as (Arany et al., 2017):

$$F_{wave} = \int_0^{h_w+\eta(t)} \frac{1}{2}C_D\rho_w Du_x|u_x|dz + \int_0^{h_w+\eta(t)} C_M\rho_w\frac{\pi D^2}{4}\frac{\partial u_x}{\partial t}dz \qquad (26)$$

$$M_{wave} = \int_0^{h_w+\eta(t)} \frac{1}{2}C_D\rho_w Du_x|u_x|zdz + \int_0^{h_w+\eta(t)} C_M\rho_w\frac{\pi D^2}{4}\frac{\partial u_x}{\partial t}zdz \qquad (27)$$

where $\rho_w = 1030 kg/m^3$ is the density of sea water, D is the outer diameter of the monopile in m, and z is the depth below the sea surface in m. $C_D = 0.7$ and $C_M = 2.0$ are the hydrodynamic drag and inertia coefficients, respectively, u_x and $\frac{\partial u_x}{\partial t}$ are the wave-induced horizontal particle velocity and acceleration, respectively, and $\eta(t)$ is the surface wave profile, h_w is the water depth, the level z is measured from the
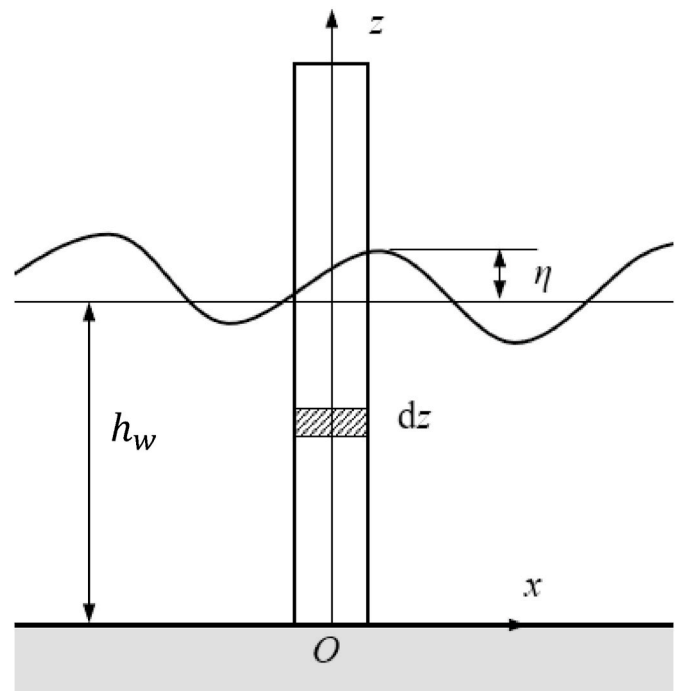

Fig. 13. The coordinate system of the Morison equation.

mudline. According to the second-order Stokes wave theory (Nei and Liu, 2002), u_x, $\frac{\partial u_x}{\partial t}$ and $\eta(t)$ are given as follows:

$$\eta(t) = \frac{H}{2}\cos(kx - wt) + \frac{\pi H^2}{4L}\left(1 + \frac{3}{2\sinh^2 kh_w}\right)coth kh_w cos2(kx - wt) \quad (28)$$

$$u_x = \frac{\pi H}{T}\frac{\cosh k(z + h_w)}{\sinh kh_w}\cos(kx - wt)$$
$$+ \frac{3}{4}\frac{\pi H}{T}\frac{\pi H}{L}\frac{\cosh 2k(z + h_w)}{\sinh^4 kh_w}cos2(kx - wt) \quad (29)$$

$$\frac{\partial u_x}{\partial t} = 2\frac{\pi^2 H}{T^2}\frac{\cosh k(z + h_w)}{\sinh kd}\sin(kx - wt) + 3\frac{\pi^2 H}{T^2}\frac{\pi H}{L}\frac{\cosh 2k(z + h_w)}{\sinh^4 kh_w}sin2(kx$$
$$- wt) \quad (30)$$

where k is the wave number in m^{-1}, w is the wave angular frequency in rad/s, L is the wavelength in m, and H and T are the wave height and period, respectively. In this study, for simplicity sake, the sum of the maximum drag and inertia forces is estimated conservatively as the design wave load (Arany et al., 2017), and the detailed calculation can be found in the study by Chang (2021).

Using the wind and wave load calculation method described above, the total bending moment for each environmental condition is calculated by M = M_{wind} + M_{wave}. The cyclic load ratio (ξ_b or ξ_b^{TY}) for each state can be obtained by dividing the ultimate bearing capacity M_R by M; then β_{TY} and α_{TY} are calculated according to Eqs. (5) and (6), and β_{cyc} and α_{cyc} are calculated according to Eqs. (8) and (9), respectively. During the service life of an offshore wind turbine, a monopile foundation would be subjected to about 10^7-10^9 load cycles due to wave and wind loads. In this paper, an average value of 10^8 was taken as the total number of cycles for the monopile throughout the design life, and then the probability of occurrence was multiplied by this average value to obtain the number of cycles for each operating condition. These values are summarized in Table 12.

5.5. Accumulation procedure

According to the Grade of Tropical Cyclones (GB/T19201-2006) (2006) recommendations, tropical cyclones with maximum mean wind speed of 32.7 m/s or higher at 10 m above mean sea level are referred to as typhoons, thus the cases from 17 to 19 presented in Table 11 are considered typhoon conditions and the other cases are non-typhoon conditions. The accumulated rotation for each typhoon and non-typhoon condition is calculated from Eqs. (4) and (7), respectively.

To determine the total accumulated rotation under typhoon and non-typhoon conditions during the design life, a rotation accumulation procedure based on Miner's rule was used, which has been validated against experimental data (Abadie, 2015; Ma et al., 2021) for predicting the accumulated rotation under load series of varying amplitudes in previous studies (LeBlanc et al., 2010b; Wang and Larsen., 2019). The total accumulated rotation of a monopile subjected to a series of load packets with different load characteristics can be calculated as follows:

Iterations $i = 1, 2, ..., n$

$$\tilde{\theta}_i = \beta_i(\xi_{b,i})N_i^{\alpha_i(\xi_{b,i})}\cdot\tilde{\theta}_{s,i}$$

$$N_{i+1}^{i,eq} = \left(\frac{\tilde{\theta}_i}{\beta_{i+1}(\xi_{b,i+1})\tilde{\theta}_{s,i+1}}\right)^{\frac{1}{\alpha_{i+1}(\xi_{b,i+1})}} \quad (31)$$

$$\tilde{\theta}_{i+1} = \beta_{i+1}(\xi_{b,i+1})\left(N_{i+1} + N_{i+1}^{i,eq}\right)^{\alpha_{i+1}(\xi_{b,i+1})}\cdot\tilde{\theta}_{s,i+1}$$

where i is the serial number of the load state from 1 to n, $\tilde{\theta}_i$ is the normalized total accumulated rotation to the ith load state, $\tilde{\theta}_{i+1}$ is the normalized total accumulated rotation to the $(i+1)$th load state, $\tilde{\theta}_{s,i}$ $\tilde{\theta}_{s,i+1}$ are the normalized static monotonic rotation to ith $(i+1)$th load state, N_i is the number of load cycles to the ith load state, $N_{i+1}^{i,eq}$ is the equivalent number of load cycles, and β_i and α_i are parameters calculated from Eqs. (5) and (6) or Eqs. (8) and (9), respectively.

6. Results and discussion

Following the monopile rotation accumulation procedure described above, the normalized total accumulated rotation under both typhoon and non-typhoon conditions and under typhoon conditions only is presented in Tables 13 and 14 as $\tilde{\theta}_{total} = 0.006129$ (0.6651°) and $\tilde{\theta}_{TY} = 0.006103$ (0.6626°). Then the parameter K_{TYC} from Eq. (10) was obtained as $K_{TYC} = \tilde{\theta}_{total}/\tilde{\theta}_{TY} = 1.00426$. This indicates that the total accumulated rotation of monopiles during the design life is mainly caused by typhoon loads. This finding is consistent with Ma's previous results (Ma et al., 2021). This phenomenon has also been found in other studies in recent years (Barari et al., 2017; Wang and Larsen, 2019). As shown in Table 13, the normalized monotonic rotation $\tilde{\theta}_s^{\xi_b^{max}}$ corresponding to the maximum cyclic load magnitude in the typhoon loading sequence ($\xi_b^{max} = 0.7$) is 0.004643, and then the parameter K_{TYS} from Eq. (11) was obtained as $K_{TYS} = \tilde{\theta}_{TY}/\tilde{\theta}_s^{\xi_b^{max}} = 1.314$. To date, few other studies have mentioned this parameter, and therefore it is not directly

Table 12
Relevant parameters of cyclic loads for all load cases.

Load case	M_{tower} (MN.m)	M_{rotor} (MN.m)	M_{wave} (MN.m)	M (MN·m)	ξ_b (ξ_b^{TY})	N	β_{CYC} (β_{TY})	α_{CYC} (α_{TY})
1	0.12	0.02	3.42	3.56	0.003	4252236	0.161	0.135
2	10.12	0.20	7.88	18.20	0.015	12637330	0.181	0.137
3	28.10	0.56	10.75	39.41	0.033	18171325	0.212	0.139
4	55.08	1.09	12.99	69.16	0.058	19447107	0.254	0.143
5	65.36	1.81	14.92	82.08	0.068	17002743	0.272	0.144
6	53.47	2.70	16.77	72.94	0.061	12576360	0.259	0.143
7	45.25	3.77	18.68	67.70	0.056	8000406	0.252	0.143
8	39.21	5.02	20.78	65.01	0.054	4415739	0.248	0.142
9	34.60	6.45	23.28	64.33	0.054	2125292	0.247	0.142
10	42.38	8.06	26.23	76.67	0.064	894,684	0.264	0.144
11	51.78	9.84	29.93	91.55	0.076	330,033	0.286	0.145
12	62.11	11.80	34.75	108.67	0.091	106,799	0.310	0.147
13	73.38	13.95	41.31	128.64	0.107	30,338	0.338	0.150
14	85.59	16.27	50.10	151.96	0.127	7568	0.371	0.152
15	98.74	18.77	61.71	179.22	0.149	1658	0.410	0.155
16	112.83	21.44	77.15	211.42	0.176	319	0.456	0.159
17	127.86	24.30	97.82	249.98	0.208	54	0.985	0.153
18	143.83	27.34	125.67	296.83	0.247	8	0.937	0.160
19	160.73	30.55	163.23	354.51	0.295	1	0.878	0.170

Table 13
Calculation results of accumulated rotation for all load cases.

Load case	ξ_b (ξ_b^{TY})	N_i	$\widetilde{\theta}_i$	$\widetilde{\theta}_{s,i}$	$N_{i+1}^{i,eq}$	$\widetilde{\theta}_N$
1	0.003	4252236	3.14228E-05	2.48531E-05	4252236	3.14228E-05
2	0.015	12637330	0.000270396	0.00015896	1.876180021	0.000270396
3	0.033	18171325	0.000830767	0.000382541	5763.74664	0.000830803
4	0.058	19447107	0.002019103	0.000724754	38659.6015	0.002019675
5	0.068	17002743	0.00264538	0.000880548	2617774.604	0.002700589
6	0.061	12576360	0.002073038	0.000769966	79736876.21	0.00275782
7	0.056	8000406	0.001717223	0.00070738	221840310.9	0.002771787
8	0.054	4415739	0.001476997	0.0006756	368537216.6	0.002776488
9	0.054	2125292	0.001308393	0.000667492	422028238.8	0.002778472
10	0.064	894684	0.00154241	0.000814859	53883241.04	0.002785051
11	0.076	330033	0.001804609	0.000996824	6535594.102	0.002805062
12	0.091	106799	0.002066199	0.001211203	851045.6014	0.002854335
13	0.107	30338	0.002324144	0.001467154	119826.1066	0.002952345
14	0.127	7568	0.002566218	0.001773029	18998.31845	0.003106987
15	0.149	1658	0.002776461	0.002138693	3418.639123	0.00330388
16	0.176	319	0.002944438	0.002580466	657.8168701	0.003518371
17	0.208	54	0.005657958	0.003121614	2.410391804	0.005695942
18	0.247	8	0.00496247	0.003794481	18.87501939	0.00602786
19	0.295	1	0.004102352	0.004642979	10.05335904	0.006129432

Table 14
Calculation results of accumulated rotation of typhoon load cases.

Load case	ξ_b^{TY}	N_i	$\widetilde{\theta}_i$	$\widetilde{\theta}_{s,i}$	$N_{i+1}^{i,eq}$	$\widetilde{\theta}_N$
17	0.208	54	0.005657958	0.003121614	54	0.005657958
18	0.247	8	0.00496247	0.003794481	18.10392045	0.005999768
19	0.295	1	0.004102352	0.004642979	9.78034583	0.006103574

comparable in the existing literature. Wang and Larsen (2019) predicted the permanent accumulated rotation of an offshore monopile during an extreme storm. A DTU 10-MW wind turbine supported by a 7.5 m diameter monopile located at 33 m water depth and three embedded lengths of 30, 35, and 40 m below the seabed with a relative density of 0.38 in medium dense sand was investigated. The storm was divided into a total of 19 sea states based on the mean wind speed, the static bending moment capacity of the monopile was calculated using the p-y model, and the method proposed by LeBlanc et al. (2010a) and Miner's law were used to calculate the permanent accumulated rotation under variable cyclic loadings. The ratio of permanent accumulated rotation to static rotation for the largest moment in the typhoon sequence $\widetilde{\theta}_{TY}/\widetilde{\theta}_s^{\xi_b^{max}}$ is 2.95, 2.16, and 1.67 for the three embedded lengths of 30 m, 35 m, and 45 m, respectively. This reveals a significant decreasing trend of $\widetilde{\theta}_{TY}/\widetilde{\theta}_s^{\xi_b^{max}}$ as the ratio of embedded length to monopile diameter increases (i.e., from 4 to 5.33). In this paper, the ratio of embedded length to monopile diameter is 6 and $\widetilde{\theta}_{TY}/\widetilde{\theta}_s^{\xi_b}$ is 1.314, which is smaller than the result of Wang and Larsen (2019) (2.95–1.67), but is in line with the decreasing trend.

According to the method proposed in this paper for estimating the permanent accumulated rotation, only three parameters, namely K_{TYC}, K_{TYS}, and $\widetilde{\theta}_s^{\xi_b^{max}}$, should be determined. Among them, $\widetilde{\theta}_s^{\xi_b^{max}}$ can be obtained by the static analysis method familiar to engineers. K_{TYC} has little effect on the total permanent accumulated rotation, so K_{TYS} is a key parameter for accurate estimation of the permanent accumulated rotation. In summary, the value of K_{TYS} is related to many factors such as site-specific metocean conditions, soil properties, geometry of structures, wind turbine size and monopile embedded length. For the designated sea area, it is necessary to analyze a large number of cases to obtain reasonable values of K_{TYS}.

It should be noted that the two coefficients in Eq. (12) are determined based on the site conditions of the South China Sea. To use this formula to estimate the permanent accumulated rotation of monopile foundations located in other offshore wind farms, these two coefficients

in Eq. (12) should be determined based on the corresponding site conditions. Other possible typhoon load series models are also of interest in future work. Further validation of the results and findings using large-scale instrumented field tests and further investigation of the mechanics underlying the findings using advanced numerical modeling technique are worthwhile. Further studies are needed to clarify the effect of settlement on the accumulated rotation of the monopile.

7. Conclusions

This paper presents the results of a series of model tests aimed at investigating the effect of typhoons on the accumulated deformation of monopiles in offshore wind turbines and a simple method for estimating the permanent accumulated rotation of monopiles during the turbine lifetime. The main findings and conclusions of the study can be summarized as follows:

(1) The results of cyclic load tests show that the accumulated rotation of the monopile under both typhoon load sequences and long-term cyclic small magnitude load sequences is suitable for estimation by a power function (LeBlanc et al., 2010a). The cyclic accumulation rate is highly dependent on the load characteristics. Miner's linear cumulative rule can provide a reasonable approximation for the permanent accumulated rotation induced by multi-amplitude loading sequences.

(2) During the design period, the total accumulated rotation of the monopile was mainly caused by typhoon events. Compared with the accumulated rotation induced by typhoon load sequences, the static rotation generated by the maximum load magnitude among typhoon load sequences is smaller, but not much different, and may maintain a certain proportional relationship.

(3) The proposed method for calculating the permanent accumulated rotation of the monopile in this paper is convenient for engineers to use in design, and its accuracy mainly depends on whether K_{TYS} is reasonable or not.

(4) The process of determining each parameter in $\widetilde{\theta}_{total} = K_{TYc}K_{TYS}\widetilde{\theta}_s^{\xi_b^{max}}$ is illustrated by means of a NREL 5-MW wind turbine mounted on a monopile in 28 m water depth in the northern part of the South China Sea. This process can also be used for other engineering cases to determine these parameters.

CRediT authorship contribution statement

Hongwang Ma: Methodology, Case study, Writing – original draft. **Xuening Chang:** 1-g laboratory floor experiment, Data curation, Case study. **Yawen Deng:** 1-g laboratory floor experiment. **Jun Yang:** Review.

Declaration of competing interest

The authors declare that they have no known competing financial interests or personal relationships that could have appeared to influence the work reported in this paper.

Data availability

Data will be made available on request.

Acknowledgments

Notation

A_b	projected area of three blades
A_R	sweeping area of the blades
C_M, C_D	hydrodynamic inertia and drag coefficient
C_T	thrust coefficient
D	outer diameter of the pile
E_{soil}	Young's modulus of the soil
F_{thrust}	thrust force on the rotor
$F_{tower}^{H_i}$	wind load acting on height of H_i
h_w	water depth
H_r	reference height
H_s	effective wave height
H_{hub}	hub height
k, L	wave number, length
K_{TYC}, K_{TYS}	dimensionless parameters
N	number of load cycles
$N_{i+1}^{i,eq}$	equivalent number of load cycles
M_{wind}	bending moment at mudline by wind
M_{wave}	bending moment at mudline by wave
M_{max}, M_{min}	maximum and minimum amplitude of the cyclic loading
M_R	ultimate moment capacity of the monopile
$\widetilde{M}_R$	normalized ultimate moment capacity of the monopile
T	wave period
$V_{W,10}$	mean wind speed at the height of 10 m
$V_{W,hub}$	mean wind speed at the hub height
w	wave circular frequency in rad/s
ρ_w	sea water density
ρ_a	air density
ξ_b, ξ_c	cyclic load characteristic parameters
ξ_b^{TY}	cyclic load ratio of typhoon load sequence
ξ_b^{max}	maximum cyclic load ratio of typhoon load sequences
$\widetilde{\theta}_{TY}, \widetilde{\theta}_{CYC}$	normalized accumulated rotation
$\widetilde{\theta}_{s,TY} \ \widetilde{\theta}_{s,CYC}$	normalized monotonic static rotation
$\widetilde{\theta}_{total}$	normalized total permanent accumulated rotation
$\widetilde{\theta}_s^{\xi_b^{max}}$	normalized monotonic static rotation corresponding ξ_b^{max}
α_1, β_1	shape and scale parameters of wind speed
β_{TY}, α_{TY}	dimensionless functions for typhoon accumulated rotation
$\beta_{cyc}, \alpha_{cyc}$	dimensionless functions for typhoon-free accumulated rotation

References

Abadie, C.N., 2015. Cyclic Lateral Loading of Monopile Foundations in Cohesionless Soils. Ph.D. thesis. University of Oxford, Oxford.

Abadie, C.N., Byrne, B.W., Houlsby, G.T., 2019. Rigid pile response to cyclic lateral loading: laboratory tests. Geotechnique 69 (10), 863–876.

Abdel-Rahman, K., Achmus, M., 2005. Finite element modelling of horizontally loaded monopile foundations for offshore wind energy converters in Germany. In:

Proceedings of the International Symposium on Frontiers in Offshore Geotechnics. ISFOG, Perth, Australia, pp. 391–396.

Achmus, M., Kuo, Y.S., Abdel-Rahman, k., 2009. Behavior of monopile foundations under cyclic lateral load. Comput. Geotech. 36, 725–735.

Achmus, M., Thieken, K., Saathoff, J.E., Terceros, M., Albiker, J., 2019. Un-and reloading stiffness of monopile foundation in sand. Appl. Ocean Res. 84, 62–73.

API, 2014. Recommended Practice 2GEO-Geothchnical and Foundation Design Considerations, twenty-second ed. American Petroleum Institute, Washington, RP2A-WSD.

Arany, L., Bhattacharya, S., Macdonald, J., Hogan, S.J., 2017. Design of monopiles for offshore wind turbines in 10 steps. Soil Dynam. Earthq. Eng. 92, 126–152.

Arshad, M., O'Kelly, B.C., 2016. Analysis and design of monopile foundations for offshore wind-turbine structures. Mar. Georesour. Geotechnol. 34 (6), 503–525.

Barari, A., Bagheri, M., Rouainia, M., Ibsen, L.B., 2017. Deformation mechanisms for offshore monopiles foundations accounting for cyclic mobility effects. Soil Dynam. Earthq. Eng. 97, 439–453.

Bisoi, S., Haldar, S., 2014. Dynamic analysis of offshore wind turbine in clay considering soil-monopile-tower interaction. Soil Dynam. Earthq. Eng. 63, 19–35.

Byrne, B.W., Burd, H.J., Zdravkovic, L., Abadie, C.N., Houlsby, G.T., Jardine, R.J., Martin, C.M., McAdam, R.A., Andrade, M.P., Pedro, A.M.G., Potts, D.M., Taborda, D. M.G., 2019. PISA Design Methods for Offshore Wind Turbine Monopiles. Offshore Technology Conference, Houston, Texas.

Chang, X.N., 2021. Simplified Calculating Method for Estimating the Accumulated Deformation of Monopile Foundations for Offshore Wind Turbine, Master Thesis. Shang Hai Jiao Tong University.

Cuéllar, P., 2011. Pile Foundation for Offshore Wind Turbines: Numerical and Experimental Investigations on the Behaviour under Short-Term and Long-Term Cyclic Loading. Ph.D. thesis, Federal Institute for Materials Research and Testing, Berlin.

DNVGL, 2016. DNVGL-ST-0437-Loads and Site Conditions for Wind Turbines. Det Norske Veritas, Oslo.

DNVGL, 2018. DNVGL-ST-0126-Support Structures for Wind Turbines. Det Norske Veritas, Oslo.

EAU, 2012. Recommendations of the Committee for Waterfront Structures, Harbours and Waterways. Ernst & Sohn, Berlin.

Fan, H.Y., 2016. Dynamics and Fatigue Analysis on Monopile Foundation of Offshore Wind Turbine under Wind and Wave Loads, Master Thesis. Harbin Institute of Technology, China.

Frick, D., Achmus, M., 2020. An experimental study on the parameters affecting the cyclic lateral response of monopiles for offshore wind turbines in sand. Soils Found. 60, 1570–1587.

GB/T19201-2006, 2006. Grade of Tropical Cyclones. Standards Press of China, Bei Jing.

GB/T50123-1999, 2015. Standard for Soil Test Method. China Architecture & Building Press, Bei Jing.

Gupta, B.K., Basu, D., 2020. Offshore wind turbine monopile foundations: design perspectives. Ocean Eng. 213, 107514.

He, J.H., Zhang, H.B., 2012. On relationship between wind speed and wave height in dynamic coupling analysis. SHIP&BOAT 23 (2), 11–16.

Jalbi, S., Arany, L., Salem, A., Cui, L., Bhattacharya, S., 2019. A method to predict the cyclic loading profiles (one-way or two-way) for monopile supported offshore wind turbines. Mar. Struct. 63, 65–83.

Jonkman, J., Butterfield, S., Musial, W., Scott, G., 2009. Definition of a 5-MW Reference Wind Turbine for Offshore System Development. Technical Report NREL/TP-500-38060.

Klinkvort, R.T., Hededal, O.H., 2013. Lateral response of monopile supporting an offshore wind turbine. Geotech. Eng. 166 (GE2), 147–158.

Le, V.H., Remspecher, F., Rackwitz, F., 2021. Development of numerical models for the long-term behaviour of monopile foundations under cyclic loading considering the installation effects. Soil Dynam. Earthq. Eng. 150, 106927.

LeBlanc, C., Houlsby, G.T., Byrne, B.W., 2010a. Response of stiff piles in sand to long-term cyclic lateral loading. Geotechnique 60 (2), 79–90.

LeBlanc, C., Houlsby, G.T., Byrne, B.W., 2010b. Response of stiff piles to random two-way lateral loading. Geotechnique 60 (9), 715–721.

Li, W.C., Igoe, D., Gavin, K., 2015. Field tests to investigate the cyclic response of monopiles in sand. Geotech. Eng. 168 (GE5), 407–421.

Li, Q., Gavin, K., Askarinejad, A., 2020. Lateral response of rigid monopiles subjected to cyclic loading: centrifuge modelling. Geotech. Eng. https://doi.org/10.1680/jgeen.20.00088.

Liao, F., Deng, H., Zeng, L., Pak-wai, C., 2018. The probability distribution of sea surface wind speeds over the northern South China Sea. Hai Yang Xue Bao 40 (5), 37–47.

Long, Y.Q., Bao, S.H., 1988. Structural Mechanics. Higher Education Press, Beijing, China.

Ma, H.W., Yang, J., Chen, L.Z., 2017. Numerical analysis of the long-term performance of offshore wind turbines supported by monopiles. Ocean Eng. 136, 94–105.

Ma, H.W., Lu, Z.Y., Li, Y.T., Chen, C., Yang, J., 2021. Permanent accumulated rotation of offshore wind turbine monopile due to typhoon-induced cyclic loading. Mar. Struct. 80, 103079.

Nanda, S., Arthur, I., Sivakumar, V., Donohue, S., Bradshaw, A., Keltai, R., Gavin, K., Mackinnon, P., Rankin, B., Glynn, D., 2017. Monopiles subjected to uni- and multi-lateral cyclic loading. Geotech. Eng. 170 (GE3), 246–258.

Nei, W., Liu, Y.Q., 2002. Dynamic Analysis of Offshore Engineering Structures. Harbin Engineering University Press, China.

Nicolai, G., Ibsen, L.B., 2014. Small-scale testing of cyclic laterally loaded monopiles in dense saturated sand. Journal of Ocean and Wind Energy 1 (4), 240–245.

Rathod, D., Nigitha, D., Krishnanunni, K.T., 2021. Experimental investigation of the behavior of monopile under asymmetric two-way cyclic lateral loads. Int. J. GeoMech. 21 (3), 06021001.

Richards, I.A., Byrne, B.W., Houlsby, G.T., 2020. Monopile rotation under complex cyclic lateral loading in sand. Geotechnique 70 (10), 916–930.

Richards, I.A., Bransby, M.F., Byrne, B.W., Gaudin, C., Houlsby, G.T., 2021. Effect of stress level on response of model monopile to cyclic lateral loading in sand. J. Geotech. Geoenviron. Eng. 147 (3), 04021002.

Schafhirt, S., Page, A., Eiksund, G.R., Muskulus, M., 2016. Influence of soil parameters on the fatigue lifetime of offshore wind turbines with monopile support structure. Energy Proc. 94, 347–356.

Shu, F.F., Ye, X.H., Liao, K.M., Feng, W.B., 2012. Distribution characteristics of wave in the Guangdong Yangxi offshore. J. Oceanogr. Taiwan Strait 31 (3), 324–331.

Tang, M.Q., Yang, Y., Jia, B., Li, C., 2018. Anti-typhoon technology research of offshore wind turbine. Electr. power 51 (2), 112–117.

Truong, P., Lehane, B.M., Zania, V., Klinkvort, R.T., 2019. Empirical approach based on centrifuge testing for cyclic deformations of laterally loaded piles in sand. Geotechnique 69 (2), 133–145.

Utsunomiya, T., Satp, I., Shiraishi, T., Inui, E., Ishida, S., 2014. Floating offshore wind turbine, nagasaki, Japan. The Series Ocean Engineering & Oceanography 3, 129–155.

Wang, S.F., Larsen, T.J., 2019. Permanent accumulated rotation of an offshore monopile wind turbine in sand during a storm. Ocean Eng. 188, 106340.

Wang, L.Z., Zhu, B., Lai, X.H., 2015. Cyclic accumulative deformation of sand and its explicit model. Chin. J. Geotech. Eng. 37 (11), 2024–2029.

van der Tempel, J., 2006. Design of Support Structure for Offshore Wind Turbines. PhD Thesis. Delf University of Technology, Netherland.

Wang, H., Ke, S.T., Wang, T.G., Kareem, A., Hu, L., Ge, Y.J., 2022. Multi-stage typhoon-induced wind effects on offshore wind turbines using a data-driven wind speed field model. Renew. Energy 188, 765–777.

Xiang, C.Y., Wu, L.G., Wei, T., Liu, Q.Y., 2016. Applications of MTCSWA data to the characteristic analysis of tropical cyclone structure. Meteorol. Mon. 42 (11), 1315–1324.